CHAPTER II

Alloy Development by Design

Abstract

A systematic approach to alloy development is proposed as a robust tool to achieve certain material requirements and objectives. First the basic understanding of empirical rules and criterion are discussed. The importance of binary, ternary, and Thermo-Calc-generated phase diagrams is introduced, along with a few alloy designs to exemplify the design concept which gives direct guidance to an alloy prototyping process.

In the second part of the chapter, alloy development techniques are explained along with experimental results to evaluate the validity of each technique. The chapter concludes with the proposed alloy development design flow chart.

1. Introduction

During the past two decades, the number of BMG publications has grown steadily. Alloy compositions that could be cast into thick glasses were reported in several metallic

systems. Several good glass formers with exceptional stability against crystallization – especially over the temperature range from Tl, the liquidus temperature, down to Tg, the glass transition temperature – have permitted an in-depth understanding of thermodynamics and kinetics of crystallization in undercooled liquids. Such knowledge, in turn, enables scientists to formulate new and improved glass forming alloys on different metallic systems.

2. Locating the Glass Forming Region – the Theoretical Design

Several criteria, empirical rules, and parameters have been established as tools for BMG explorations. A few must be mentioned here because of their effectiveness, robustness, and most importantly, simplicity. These criteria have been tested experimentally and their prediction abilities shall be commented on based on successful results and known limitations. The following rules were employed as a guideline for choosing the alloying elements to achieve the best glass forming ability (GFA), which is understood as the ease of vitrification. Currently the two universal criteria for comparing the GFA of the liquids are (1) critical cooling rate (Rc), which is the slowest possible cooling rate to bypass the crystallization in the undercooled melt, and (2) critical casting thickness (d_c), which is the largest possible thickness to cast a fully amorphous strip. Though both entities are closely related, the critical casting thickness could easily be the most quantitatively compared entity in the BMG communities because of the simplicity of d_c characterization and the implied engineering and commercial realization. Appendix B explains the relationship between critical casting thickness and critical cooling rate.

2.1 The Reduced Glass Transition as a Quick Screening Tool

Perhaps the most powerful and yet user-friendly criterion for predicting glass forming ability is the reduced glass transition temperature (Trg)[1]. Postulated by Turnbull in 1969, Trg is equal to Tg/Tl when Tg is the glass transition temperature and Tl is the liquidus temperature. This dimensionless parameter has been used extensively as a parameter to consider glass forming ability (GFA) of most metallic glass alloy. Based on our experience, the values of Trg between two families of metallic glass alloys do not yield accurate GFA comparison. However, such GFA assessment is much more accurate if the values of Trg are compared within the family of alloy. Generally speaking, we found that Trg values between 0.50 and 0.67 indicate good GFA, and when Trg exceeds 0.6 the GFA is exceptional (e.g., 0.642 for $Zr_{41.2}Ti_{13.8}Cu_{12.5}Ni_{10}Be_{22.5}$ and 0.69 for $Pd_{40}Cu_{30}Ni_{10}P_{20}$).

It must be noted that Trg is among a few parameters that could be assessed during the early stage of alloy development (i.e., when GFA is below average). To study Trg in the alloys with nominal GFA, the melts must be rapidly quenched to obtain a glass (in our case, splat-quenched) and the values of Tg and Tl can be extracted from the differential scanning calorimetric study. If these nominal glass formers were cast into millimeter thick strips, the casts would not contain any amorphous fraction, and therefore Tg and other glass-related parameters could not be assessed.

Another parameter used extensively is ΔT, which is equal to Tx – Tg where Tx is the onset of crystallization temperature and Tg is the glass transition temperature. ΔT

represents the width of the supercooled liquid region. During the constant heating experiment in the DSC, BMG solid is heated and enters into the supercooled liquid region at Tg, where the glass relaxes. If the supercooled liquid has good stability against crystallization, there will be a large temperature window upon heating before the first crystallization event takes place, resulting in large ΔT. Therefore the ΔT parameter is viewed as a measure of the alloy's stability against crystallization and therefore of its GFA [2]. However, this relationship is not always true, as shown later in the chapter.

2.2 Glass Forming Region as the Reciprocity of Solid Solubility

Hume-Rothery rules [3, 4] are widely used criteria to determine the solid solubility of a solute element in a metal. These simple but elegant rules could be summarized as follows:

I. If the difference in atomic sizes is more than 15%, the solubility is limited.
II. Crystal structures of the two elements must be identical to establish considerable solubility.
III. Metal with lower valency is more likely to dissolve in metal with higher valency.
IV. Electronegativity difference close to nil gives maximum solubility. Large differences lead to compound formation.

Another powerful yet simple idea was introduced by Darken and Gurry, who created a map as a tool to predict solid solubility based on ionic radii and the electronegativity of metals as shown in Figure II-1. Typically an ellipse is constructed with major and minor axes corresponding to 0.4 difference in electronegativity (+0.2 to -

0.2) and 15% difference in radii (-7.5% to +7.5%) is plotted to show a high solubility domain. A larger ellipse corresponding to -0.4 to +0.4 electronegativity difference and -15% to +15% difference in radii is plotted to show solubility range.

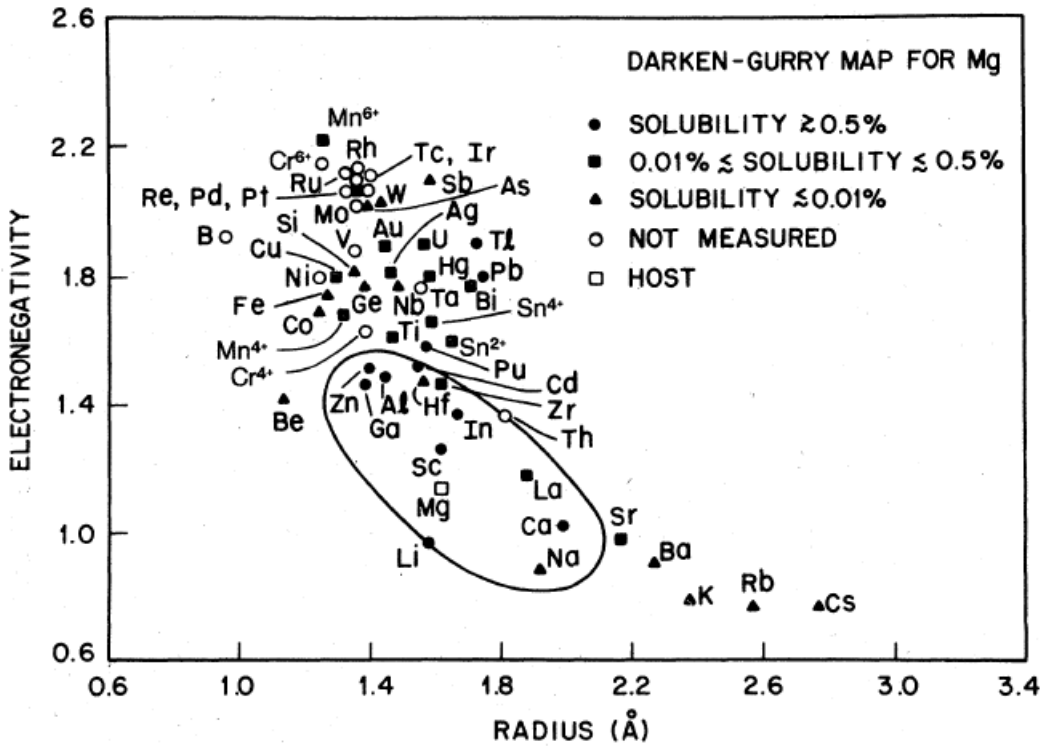

Figure II-1: Darken-Gurry map for Mg. The enclosed region around Mg is to indicate a high solubility domain (reproduced after [5]).

The limit of solid solubility is associated with the local atomic level strain as a result of atomic size differences, as well as the valence electron configurations. If the lattice can no longer support the strain caused by extended solubility, then the crystals are "frustrated." As the reciprocity of solid solubility, amorphization is the phase transformation that occurs to accommodate an overly strained crystal lattice that has reached its maximum bound for solid solubility. Such crystals are topographically

unstable. The instability in solid solution has led to an empirical theory [6] developed by Egami and Waseda, who investigated glass formation in 66 systems and demonstrated that there was a correlation between a glass forming region and atomic volume mismatch. The atomic radii shown in Figure II-2 can be found in [6]. The radii were determined directly from rapidly quenched amorphous alloys, and in some cases, from the metallic close-packed structure of the element.

Another noteworthy model based on the atomic packing and lattice topography was recently suggested by Miracle [7] who found distinct "fingerprints" in the atomic radii vs. the concentration plots in most published BMG systems. Two particular examples are shown in Figure II-3 for Zr-Ti-based BMGs and Mg-based BMGs. For both cases, there are a series of well-defined atomic radii fractions. Each of the fractions represents topologically identical solutes. For the Zr-Ti case, the size fraction decreases from 1.0 (main constituent) to 0.9, to 0.8, and then to 0.7. For the Mg case, the main constituent is 1.0 and the two atomic fractions of other alloying elements are at 0.8 and 1.1. The model provides specific guidance for selecting candidate solute elements and concentrations.

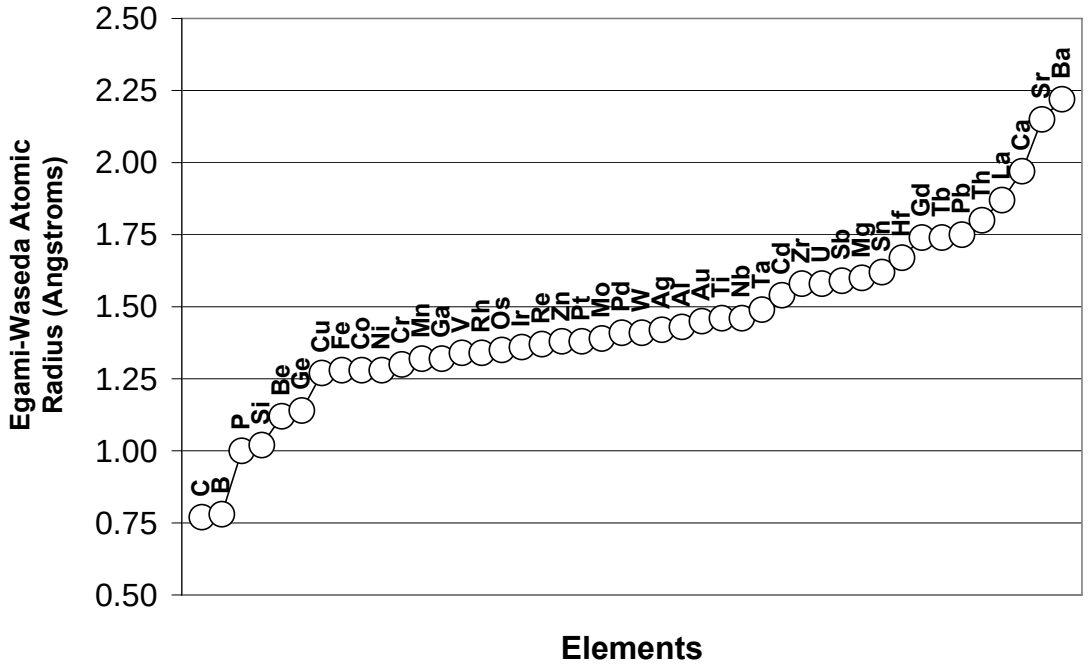

Figure II-2: Atomic radii of elements measured in amorphous alloys, and a in some cases, obtained from metallic close packed structure of the element. The numbers are tabulated in [6].

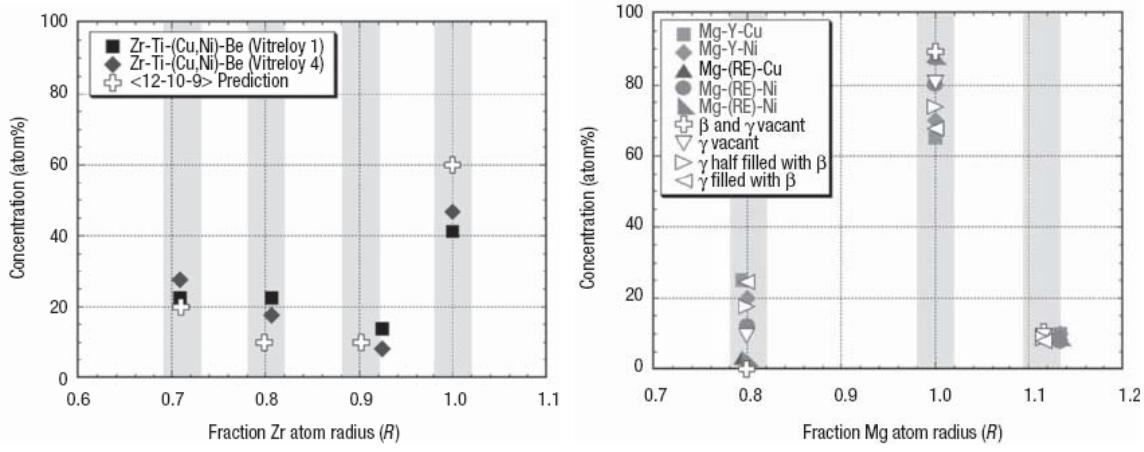

Figure II-3: Comparison of relative atomic size and concentrations for Zr-Ti-based BMGs and Mg-based BMGs. Two distinct "fingerprints" can be realized (reproduced after [7]).

2.3 Glass Forming Region at the Stability Limit of Crystalline Material

In the late 1980s, Johnson and coworkers [8-10] published a few interesting publications on the stability limit for superheated or supersaturated crystals. The proposed model was an "inverse" [10] complement to Kauzmann's argument [11] – there must be a phase change before the entropy of an undercooled liquid falls below that of the crystalline phase.

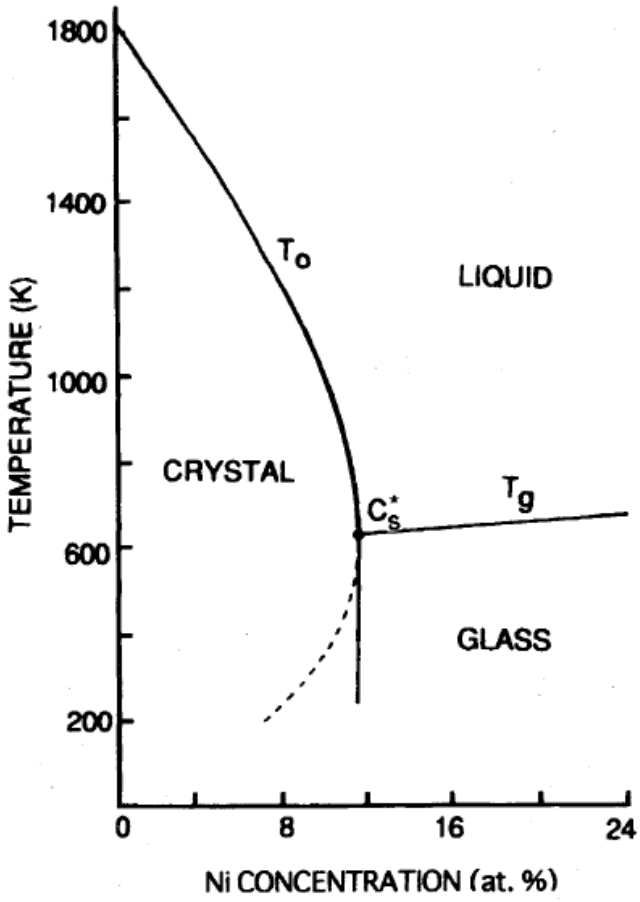

Figure II-4: Calculated polymorphous phase diagram of Ni-Zr system (reproduced after [8]). The left axis represents pure Zr concentration (Zr-rich).

Representing the coexistent of liquid, glass, and supersaturated crystal phases, the triple point is the intersection of the polymorphic melting curve (T_0 line) and the ideal glass transition curve in the temperature-composition space shown in Figure II-4. The critical concentration that commences the glass forming region could be projected from the triple point down to the composition axis. Okamoto et al. developed an enhanced technique [12] to construct the generalized polymorphous melting curve (T_0), and to locate compositional space for glass forming alloys based on generalized Lindemann Melting Criteria. An alternative approach to construct T_0 is to approximate the middle points between liquidus and solidus found at the solvent-rich side of the equilibrium binary phase diagram which is then intersected by a Tg curve which is nearly a horizontal line.

2.4 Experimental Results to Verify Theories

To test out the validity of the theories mentioned above, the author collected experimental data found in the literature for the Ti-Ni system – a core component of the Al-Ti-Ni alloy family which was later investigated extensively. It must be noted that the width of the glass forming region varies with the cooling rate of the experiment. For example, the largest width can naturally be found using ion beam mixing, thin film deposition, or solid-state transition, where the cooling rate could be as high as 10^{13}-10^{14} K/s. [13-15] For splat-quenching, the cooling rate is approximately 10^6-10^8 K/s, depending on the splat's thickness [16], and the resulting glass forming region should be narrower.

Using Egami-Waseda [6] criteria, the $Ti_{74}Ni_{26}$ was found to be maximum solubility bound. Polymorphic T_0 extrapolated curve gives $Ti_{80}Ni_{20}$ as the maximum. Molecular dynamic (MD) simulation work[A] by Lai et al. suggests $Ti_{85}Ni_{15}$ as the maximum, while their ion beam mixing experiments also showed maximum at $Ti_{85}Ni_{15}$ with 5 at% error. [17]

Our splat quenching experiments were completed on (TiZr)-Ni systems and the maximum bound was located at 65 at% Zr/Ti content (with a Zr:Ti ratio of approximately 1:3). The result is summarized in Table II-1 below. The listed percentages are Ti atomic percent (Ti-rich).

Polymorphic Melting [10, 12]	Egami-Waseda Criterion	Molecular Dynamic[A]	Ion Beam Mixing	Splat Quenching
80%	74%	85%	85% (±5% err.)	65%

Table II-1: Summary of critical Ti atomic percents in the Ti-Ni alloy system. These numbers post as the upper bounds for Ti content which is capable of amorphization.

The summary of data is also plotted in Figure II-5. There is no clear-cut answer as to which criterion is better. The accuracy seems to be dependent on the system investigated. The calculated glass forming region is viewed as just a big "sample space"

[A] In the study, the n-body potential was employed using Parrinello-Rahman MD scheme. More information can be found in [17-19].

in which a good glass former could be located. Another shortcoming of models is the lack of ability to extend the prediction in binary systems to ternary and more complex systems.

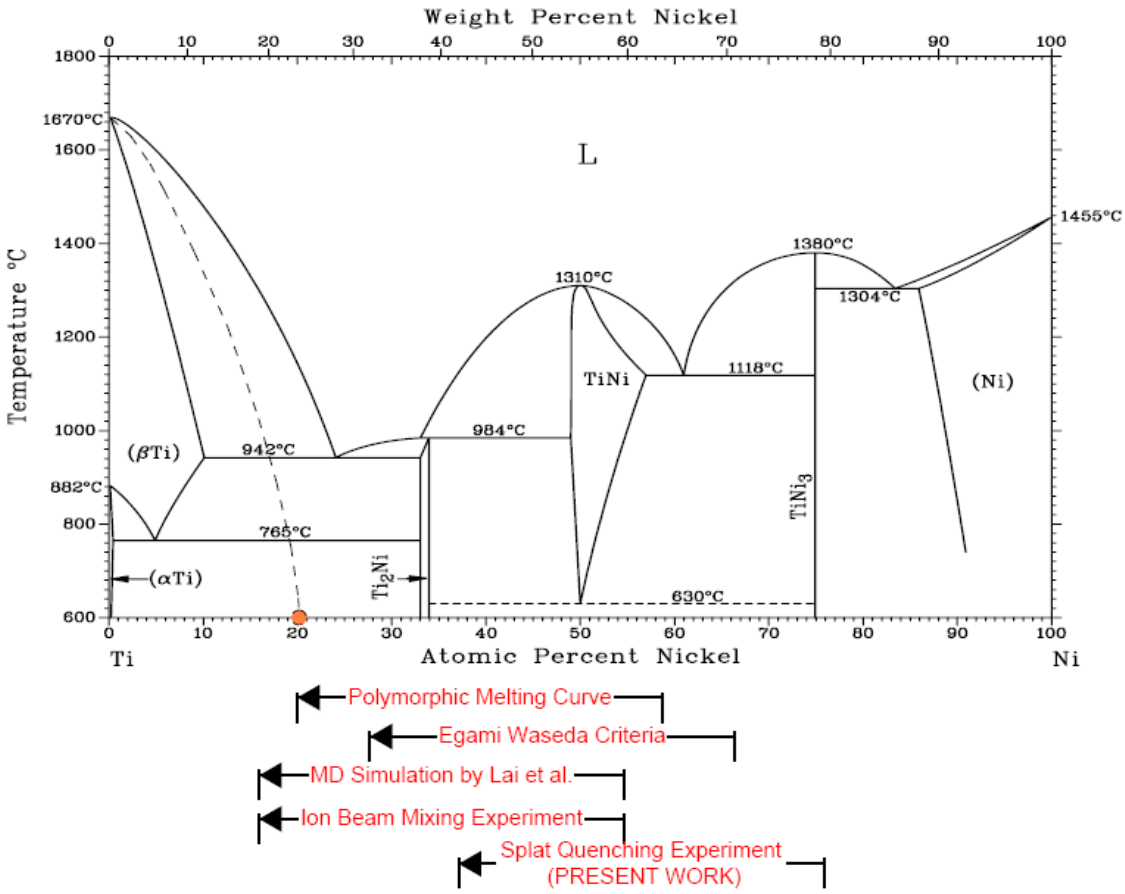

Figure II-5: The maximum bounds of a glass forming region are predicted for Ti-Ni binary phase diagram [18] using different approaches. The polymorphic melting curve is manually created by locating the middle points between solidus and liquidus lines. The arrows at the bottom show different prediction techniques and where the predicted maximum bounds for a Ti-Ni glass forming region are located in compositional space.

3. Locating the Glass Forming Region – the Practical Approaches

Here are a few techniques and practical exercises that we found to be the most efficient in quickly screening for alloys with good GFA. The explanations are given along with real examples, which were mainly collected during the development of Au-based alloy systems.[B]

3.1 Phase Diagrams

Binary and ternary phase diagrams were proven to be one of the best places to start any development process. Deep eutectics and a steeply descending liquidus feature are some of the hints available from the phase diagrams that there could be alloys with good GFA located at the respective compositions in such systems. Naturally, the liquidus temperature (T_l) reaches local minima at deep eutectics. The steeply falling liquidus curves are translating directly into the sharp raise of Trg value, because $Trg = Tg/T_l$ and Tg tends to vary slowly with compositional change.

[B] Over the course of three years (2004-2007), there were two separately-funded Au-based BMG projects at Caltech. The first project was funded by Liquidmetal Technologies and the goal was to develop Au-BMGs of 18 karat gold content. The second project was funded by Intel Corporations and the goal was to develop alternative Pb-free solder alloys that are not formulated around the poor metal group (post-transition metal group), have deep eutectic, have glass forming potential, and have a low melting point of less than 250 ^{o}C (which is the temperature range for soldering). Au-based alloys were proposed as the possible metals of choice. The details of this project will be discussed in Chapter VI.

To demonstrate the idea, the Au-based binary phase diagrams [19] have been surveyed to locate the deepest eutectics on the gold-rich terminal. The eutectic temperatures and compositions were plotted in Figure II-6 to show the T_l-reduction effect of selected alloying elements.

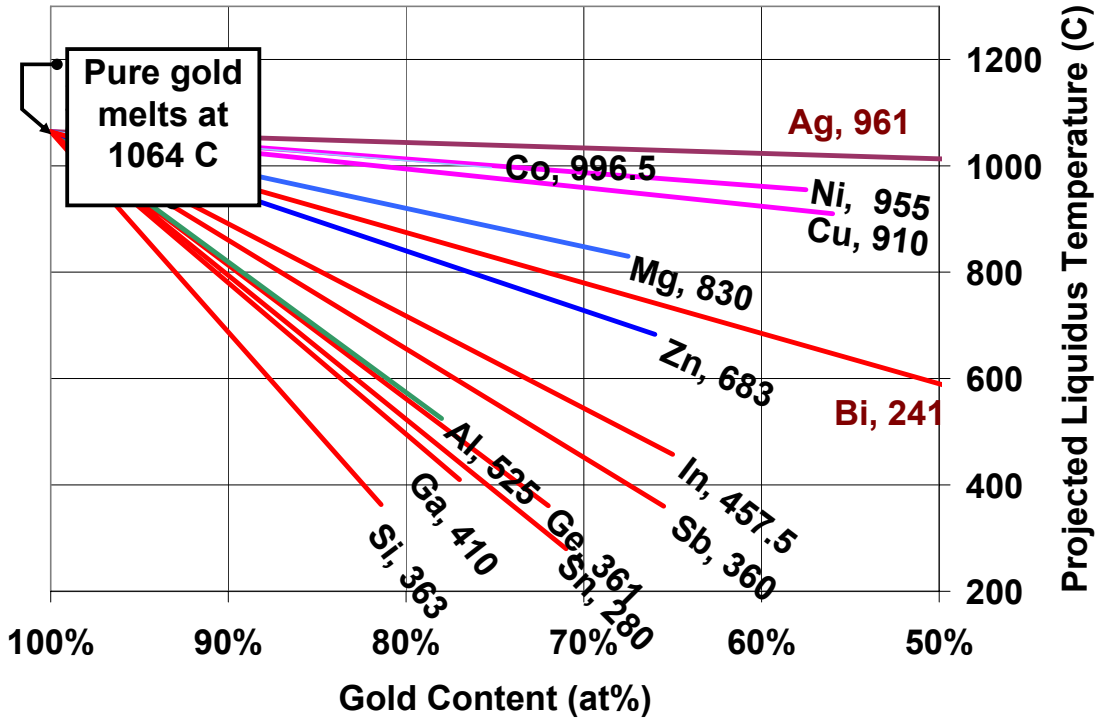

Figure II-6: Liquidus projections are plotted by extrapolation of pure gold's melting temperature to the eutectic compositions and eutectic liquidus temperatures of selected alloying elements. The effect of Si is the most pronounced. As a solute, Si is capable of dropping T_l by 700 ^oC at 19 at% content.

Based on Figure II-6, Au-Si clearly exhibits the deepest eutectic, and therefore is worth investigating. The large Egami-Waseda atomic radii[C] difference between Au (1.45 Å) and Si (1.02 Å) of ~30% is another attribute of a good glass former.

A similar approach can also be applied to ternary phase diagrams. Liquidus projection diagrams and isothermal cross-section diagrams are valuable tools in pinpointing any glass forming regions. The liquidus projection of a Au-Si-Ge ternary phase diagram is illustrated in Figure II-7 to show a deep pseudo-binary eutectic valley on the Au-rich side of the compositional space. The valley, as represented by the shaded region, confirms that the liquid of a certain composition is the stable phase below 400 ^{o}C. The phase diagram also implies that Ge could be substituted into Au-Si without significantly increasing the alloy's overall liquidus temperature.

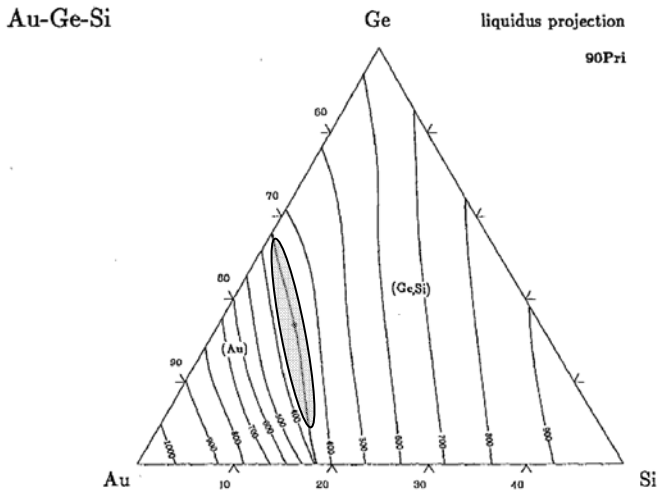

Figure II-7: Liquidus projection of Au-Ge-Si ternary diagram [20] (gold rich corner) reveals that liquid of certain alloy compositions (as shaded in the picture) has a pseudo binary eutectic valley at temperatures below 400 ^{o}C. The compositions range from $Au_{80}(Si/Ge)_{20}$ to $Au_{72}(Si/Ge)_{28}$, depending on the Si:Ge ratio.

[C] The atomic radii of Au and Si were obtained from $Pd_{80}Si_{20}$, $Au_{70}Si_{30}$, and $Au_{35}Ni_{65}$ amorphous alloys.

3.2 Thermo-Calc ™

When phase diagrams of interest are not available, Thermo-Calc software [21] could help expedite the alloy development process by generating phase diagrams which are calculated based on the available databases. In the first example, various isothermal sections for Au-Sn-Sb ternaries are calculated.[D] During the simulations, the cross-section temperature was slowly lowered until a deep eutectic composition could be located. As shown in the temperature progression in Figure 8, the size of the liquid region contracts when the temperature drops from 300 C → 275 C → 250 C. The existence of the liquid phase at a temperature as low as 250 ^{o}C suggests that such a eutectic composition could be undercooled deeply and may potentially be a good glass former.

Experiment results showed that the composition prediction was quite accurate, for example, the experimental eutectic was located at $Au_{68}Sn_{26}Sb_6$ and Thermo-Calc's prediction is at $Au_{65}Sn_{24}Sb_{11}$. However, the experimental liquidus temperature was 289 ^{o}C instead of ~250 ^{o}C as predicted.

[D] Complied using Thermo-Calc Software AB (2004) and SSOL2 database which includes:

A. Dinsdale, SGTE Data for Pure Elements, Calphad Vol 15(1991) p 317-425, also in NPL Report DMA(A)195 Rev. August 1990

P-Y Chevalier, Thermochimica Acta, 130 (1988) p 1-13; AU-SN

I. Ansara, J.P. Nabot, Caphad (in press 1990); Au-In

P-Y Chevalier, Thermochimica Acta, 155 (1989) p 211-225; AU-SB, AU-TL

P. Miodownik and N. Saunders, Lattice stabilities

B. Jonsson and J. Agren, Mater. Sci. & Techn. Vol 2(1986) p 913-916, TRITA-MAC 284 (1985); SB-SN

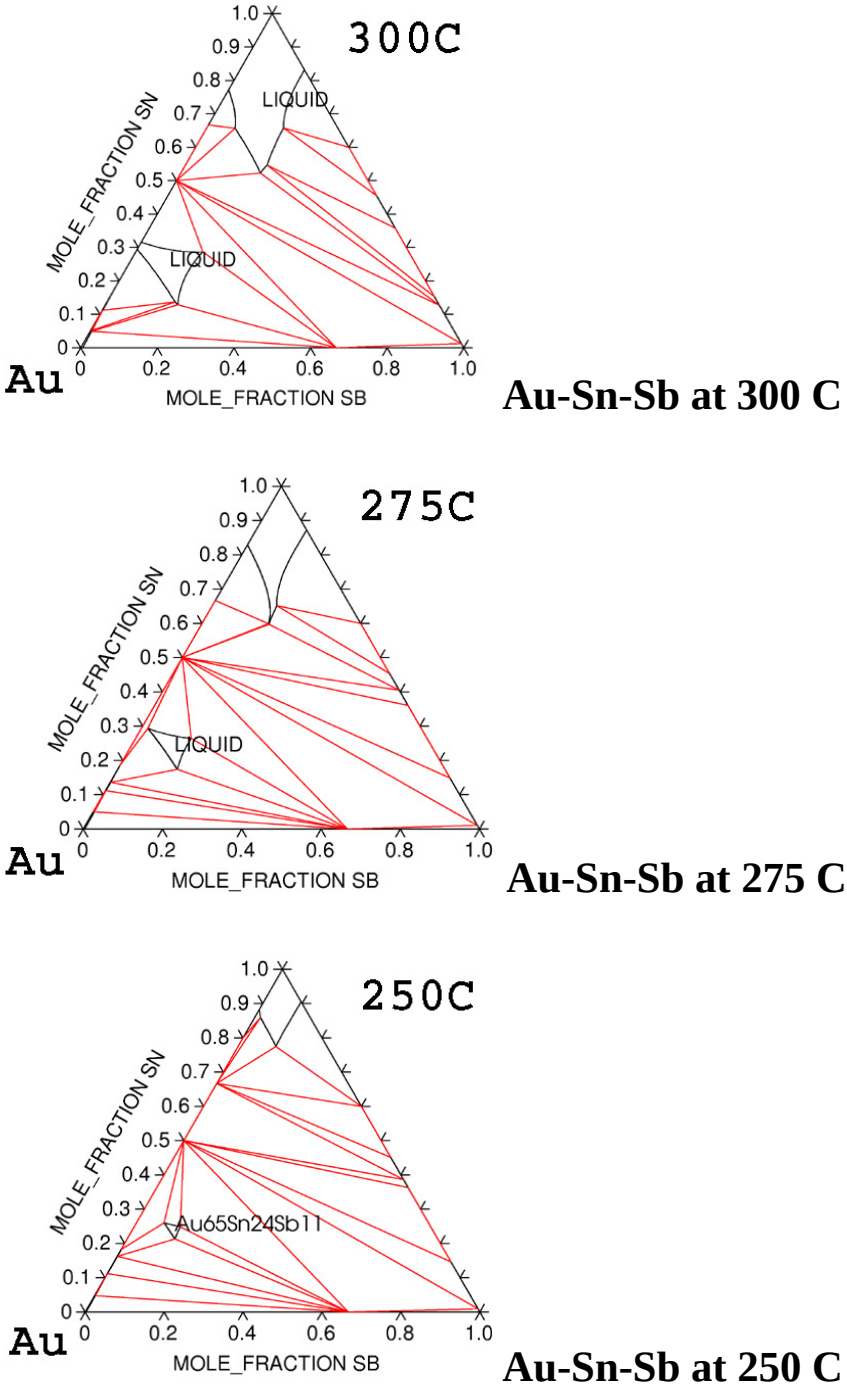

Figure II-8: Isothermal cross sections for Au-Sn-Sb ternary system were generated using Thermo-Calc. The liquid region is shrinking with the temperature evolution from 300C → 275C → 250C. The deep eutectic composition is predicted at $Au_{65}Sn_{24}Sb_{11}$.

In another example, 900 K, 950 K, and 1000 K isothermal cross sections for the Au-Cu-Si ternary diagram shown in Figure II-9 are computed using Thermo-Calc.[E] According to the prediction, the three isothermal cross sections show the evolution of a liquid "pocket" which retracts across the compositional space from the Cu-rich side to the Au-rich side. The liquid pocket represents alloy compositions that have low T_l – a good indication of GFA. The accuracy of the Thermo-Calc prediction greatly depends on the available database. For the particular case of an Au-Cu-Si system, our experimental results show that the best glass former should be located at $Au_{55}Cu_{25}Si_{20}$. The results are tabulated in Table II-2 below.

	Best Glass Forming Composition (experimental)	Best Glass Forming Area (calculated)
Composition	$Au_{55}Cu_{25}Si_{20}$ (0.5 mm)	Au 40-60, Cu 20-30, and Si 20-40
Liquidus Temp	654 K	900-950 K

Table II-2: Comparison between experiment results and Thermo-Calc predictions

[E] Complied using Thermo-Calc Software AB (2004) and SSOL2 database which includes:

A. Dinsdale, SGTE Data for Pure Elements, Calphad Vol 15(1991) p 317-425, also in NPL Report DMA(A)195 Rev. August 1990.

N. Saunders, unpublished research, COST-507, (1991); Al-Cu

I. Ansara, J.P. Nabot, Caphad (in press 1990); Au-In

I Ansara, unpublished work (1991); Cr-Si

D. Ludecke, report at KTH; CU-SI

M. Kowalski, RWTH, unpublished work (1990); Cu-Zn

P-Y Chevalier, Thermochimica Acta, 141 (1989) p 217-226; AU-GE, AU-SI'

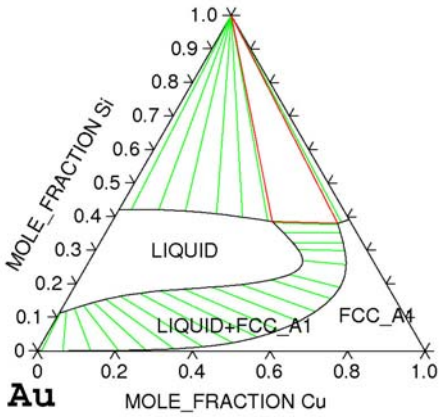

Au-Cu-Si at 1000 K

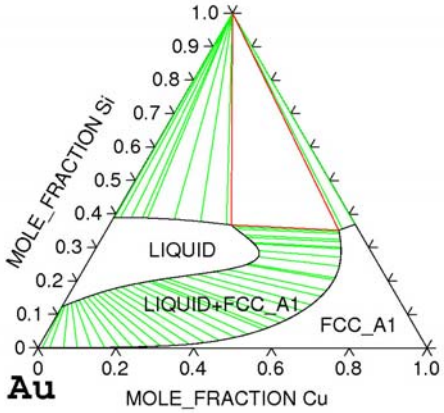

Au-Cu-Si at 950 K

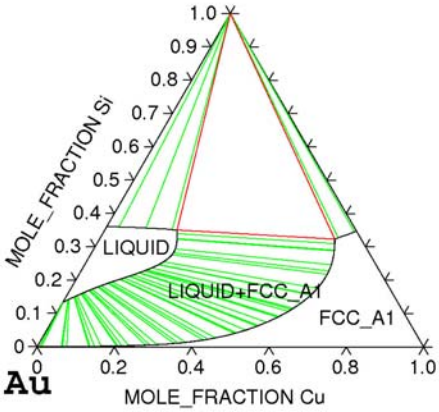

Au-Cu-Si at 900 K

Figure II-9: 1000 K, 950 K, and 900 K isothermal cross sections for Au-Cu-Si ternary system as calculated using Thermo-Calc. There exists a low melting temperature region (labeled "LIQUID") which retracts itself along compositional space towards Au-Si binary axis when the temperature drops from 1000 K → 950 K → 900 K .

Following Thermo-Calc predictions, many "promising" compositions were synthesized and splat-quenched. According to Turnbull's Trg parameter, the T_l of 900 K requires Tg to be above the 470-500 K range if this were to be a good glass. Table II-3 shows a few selected alloy compositions based on a Au-Cu-Si system, and the corresponding experimental values of Tl, Tg, Tx, and Trg.

#	Alloy Compositions	Tg (^{o}C)	Tx (^{o}C)	Tl (^{o}C)	Trg (^{o}C)
1	Au65.5 Cu15 Si19.5	63	100	500	0.43
2	Au55 Cu25 Si20	84	110	545	0.44
3	Au50 Cu30 Si20	90	116	540	0.45
4	Au44 Cu36 Si20	120	150	576	0.46
5	Au53.6 Cu24.4 Si22	80	115	615	0.398
6	Au56.4 Cu25.5 Si18	80	118	610	0.400
7	Au50 Fe5 Cu25 Si20	90	130	393	0.545
8	Au50 Ni5 Cu25 Si20	100	125	390	0.562
9	Au50 Pd5 Cu25 Si20	104	144	390	0.569

Table II-3: Selected alloy compositions based on Au-Cu-Si system are tabulated with the experimental values of Tl, Tg, Tx, and Trg.

While the temperature range prediction is not accurate enough for quantitative analysis, Thermo-Calc was proven to be useful when temperatures are compared in relative terms. To summarize the accuracy of Thermo-Calc, experimental results were plotted against Thermo-Calc predictions as shown in Figure II-10. Eight ternary eutectic compositions were located using Thermo-Calc and then systematic experiments were

conducted to narrow down the "real" eutectic compositions. Eutectic temperatures from the experiments were recorded and compared with Thermo-Calc-calculated temperatures. The diagonal solid line shown corresponds to the equation y = x (45^o slope) to show ideal agreement between Thermo-Calc and experiments. The dotted line is the true linear fit of the data which, in our case, does not deviate much from the ideal situation. The two dash lines post as lower and upper bounds for 95% confidence limit. There are only two data points that did not fit within the 95% confidence band.

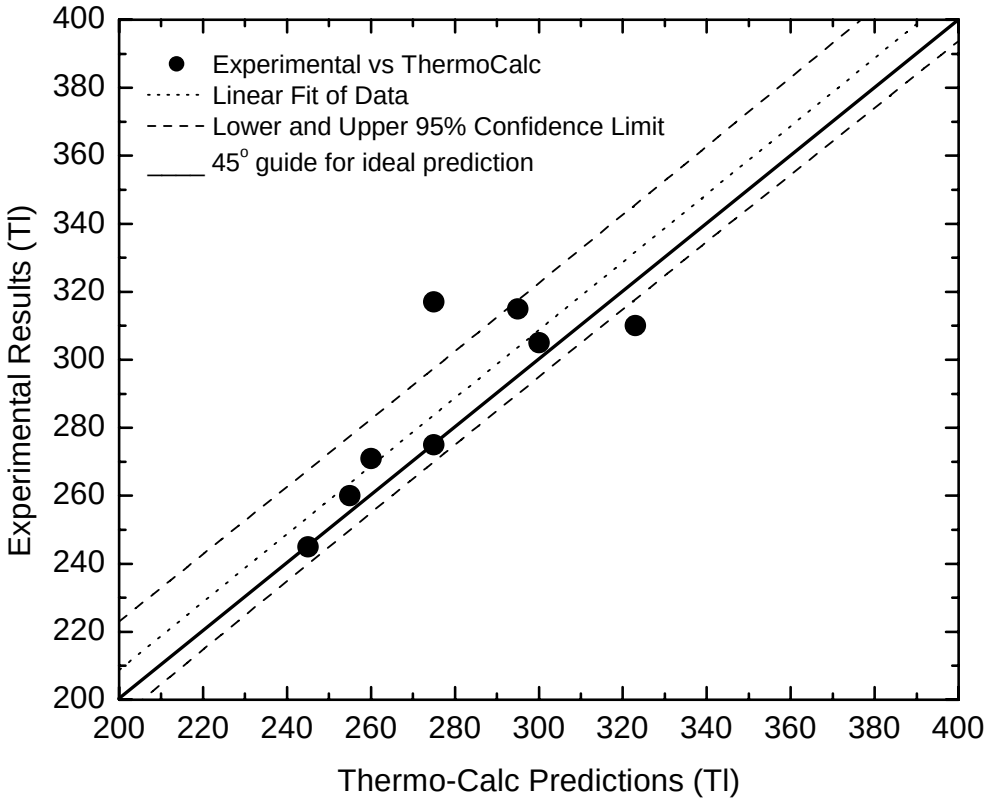

Figure II-10: The experimental liquidus temperatures of the different eutectic alloys are plotted against Thermo-Calc predictions to show dependability of Thermo-Calc.

3.3 Multi-Component Alloy Design Based on Two Eutectics

The alloy design gets more complicated as more elements are added into the system. Binary and ternary alloys can be readily represented on two-dimensional plots. However, when fourth, fifth, etc., elements are added into the alloys, different projecting or representation techniques are required to understand the effect of each alloying element with respect to the concentration.

One design framework is based on the assumption that when two different binary eutectic alloys are mixed, it is possible [22] that the two eutectics do show symbiotic effect by further lowering the liquidus temperature of the 4-component alloy system.

For example, both binary and ternary systems for Au-based alloy systems have been extensively investigated. With tremendous help from Thermo-Calc, the eutectic temperatures were located experimentally and the results are shown in Figure II-11. The bottom of the plot shows the grid that represents the second and third constituents added to the Au-based system. The two smiley faces (☺) shown in Figure II-11 represent the two chosen eutectics (Au-Sn and Au-Ge-Sb) to be tested for their symbiotic temperature lowering effect.

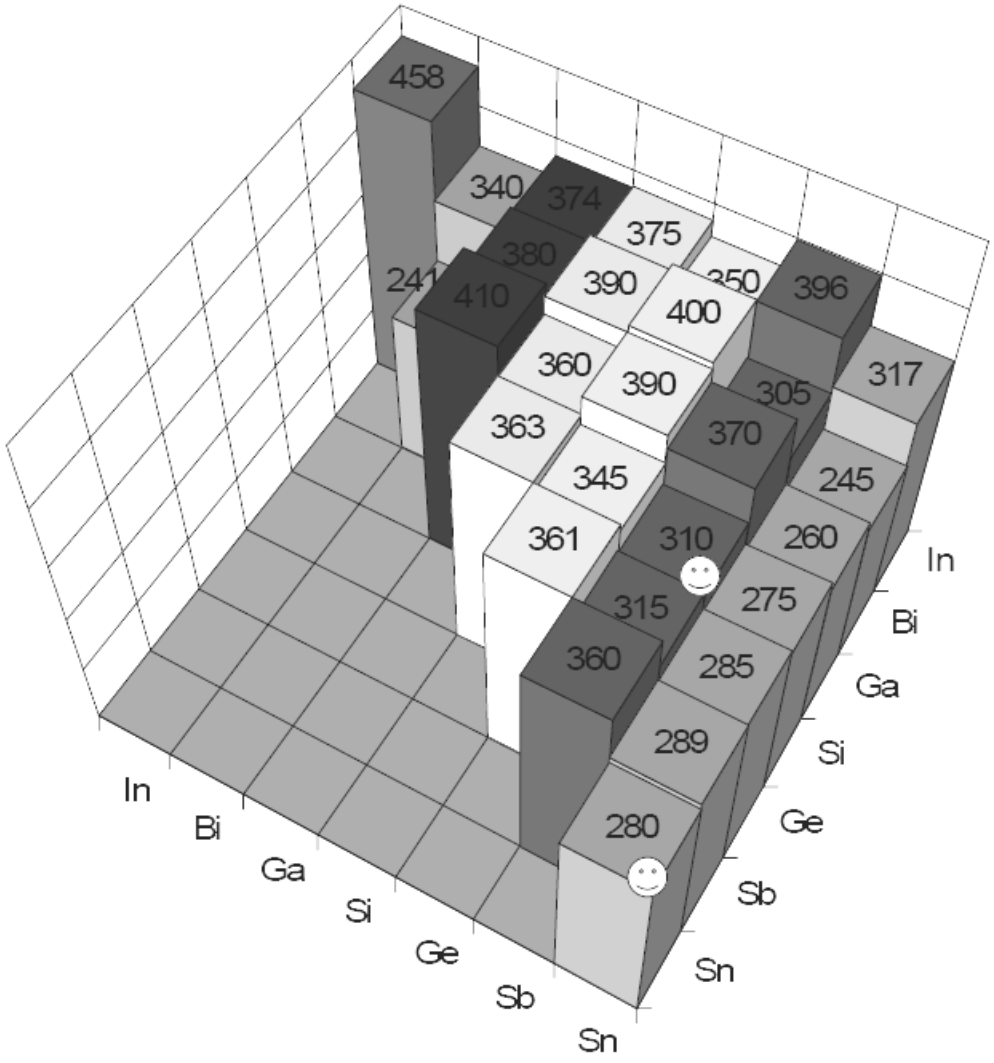

Figure II-11: Eutectic temperatures of selected Au-based binary and ternary systems. The second and third alloying elements are represented on the X and Y axis (bottom grid) while the Z-axis (height) shows the eutectic temperatures (C). The two smiley faces represent the two chosen eutectics to be tested for Symbiotic temperature lowering effect as illustrated in Figure II-12.

The concept is illustrated in Figure II-12 where the two selected eutectics are plotted on the opposing sides of the cube. The base of the cube represents the composition space, and the height (z-axis) represents the melting temperature. An imaginary line is drawn to connect the two eutectics. Using the lever rule, the compositions of the new alloys can be selected from various positions on this imaginary line. If the two eutectic systems do show a symbiotic effect, the melting temperature of the new alloy will be lower.

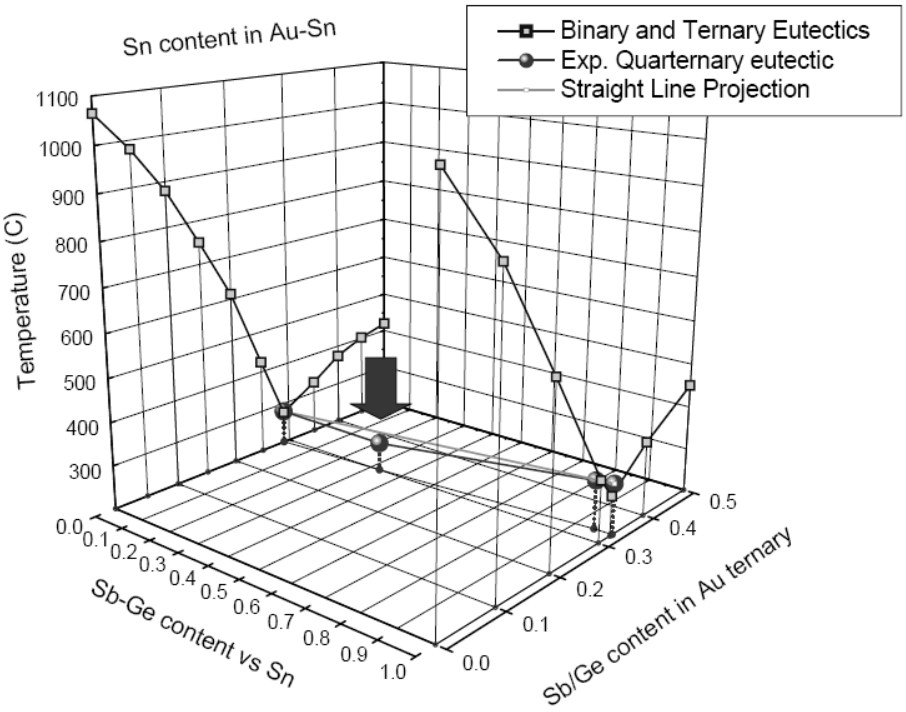

Figure II-12: A new alloy design is based on the symbiotic lowering temperature effect of two selected eutectics. The two opposing sides of the cube represent the eutectics of binary Au-Sn and ternary Au-Sb-Ge alloys. The squares represent the liquidus temperatures of the two investigated eutectics.

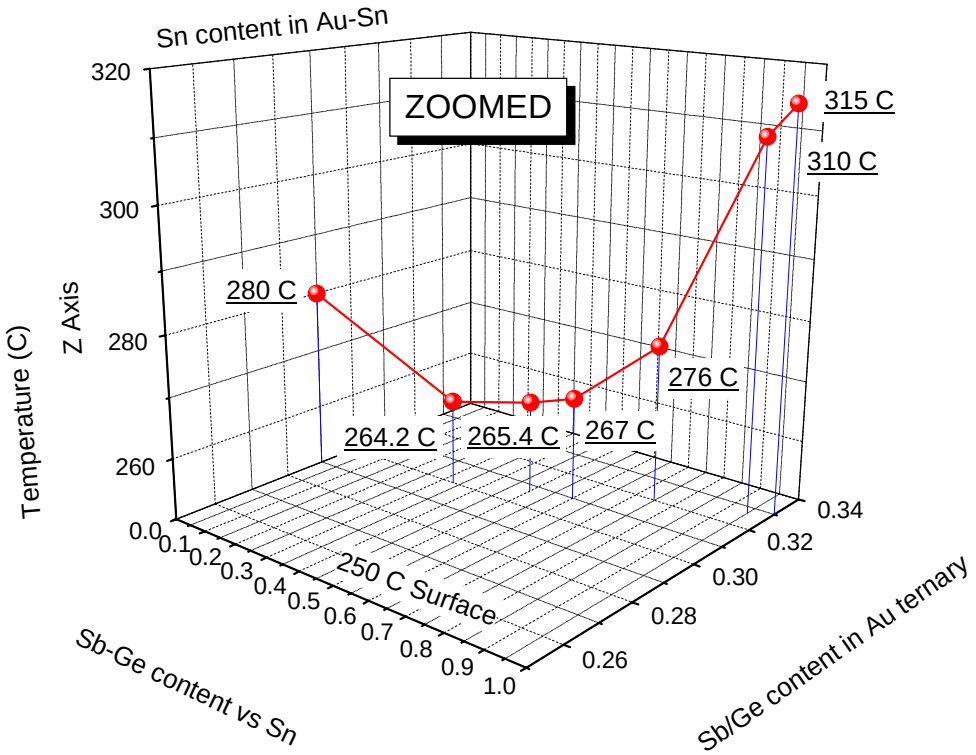

Figure II-13: The experimental results (represented by spheres) are shown using the same 3D diagram construction as shown in Figure II-12. The temperature axis is "zoomed in" to show the symbiotic temperature lowering effect by mixing binary Au-Sn and ternary Au-Sb-Ge alloys together using the lever rule $(Au_{71}Sn_{29})_{(100-X\%)}\ (Au_{67}Ge_{15}Sb_{18})_{(X\%)}$.

Experimental results are shown in Figure II-13. The melting temperature of the new alloys dropped by different magnitudes depending on the compositions. The biggest drop was approximately 16°C. The compositions of the alloys were calculated using the lever rule:

$$(Au_{71}Sn_{29})_{(100-X\%)}\ (Au_{67}Ge_{15}Sb_{18})_{(X\%)}.$$

3.4 Alloy Processing

In prior sections, the "deep" eutectic compositions in the systems of interest were predicted using thermodynamic calculations and "educated" guesses. These suggested compositions must be verified experimentally. Such experimental verification is, perhaps, the most time-and-energy consuming process in the alloy development project. With recent progress in molecular dynamic simulation (e.g., [23]) and thermodynamic calculations – together with better understanding of crystallization kinetics, phase transformation, and physics of glass formation as a whole – alloy developers can now efficiently conduct experiments at more specific alloy compositions. The experimental work can be roughly divided into two stages – *the rapid quenching stage* and *the slow quenching stage.* The second stage will be employed only if potential good glass formers are found in the first stage.

3.4.1 Rapid Quenching Stage

In the early stage of alloy development, the liquids are generally poor glass formers. Glassy phases could only be obtained by rapidly quenching from the melts. Some of the commonly used rapid quenching techniques include melt spinning [24, 25], drop tower [26, 27], atomization [28], and splat-quenching [29]. Here at Caltech, splat-quenching is the primary tool used for rapid quenching studies. Typical splat-quenched samples are 25-70 microns thick and undergo solidification at a cooling rate on the order

of $10^5 – 10^6$ K/sec.[F] Some amorphous fraction is usually found in most nominal glass formers after they are splatted. T_l, T_g, and T_x of these alloys could be obtained readily by Differential Scanning Calorimetry (DSC) study using constant heating scans. $Trg = T_g/T_l$ is generally used as a rudimentary criterion to quickly assess GFA. The heat of crystallization (ΔH_c) recorded during DSC heating scan is usually an indication of amorphous fraction in the sample. If ΔH_c is as large as 45 – 55% of the heat of fusion, then the splatted sample is generally assumed to be fully amorphous (or nearly so). The DSC analysis is usually accompanied by X-ray diffraction analysis to verify the presence or absence of crystalline and amorphous phases.

As shown in Figure II-14, the alloy compositions were slightly adjusted to confirm the liquidus trend in the $Au_XCu_{80-X}Si_{20}$ isopleth, as predicted by Thermo-Calc (Figure II-15). The Si content is fixed at 20 atomic% while Au and Cu contents are varied according to the formula $Au_XCu_{80-X}Si_{20}$. Experimental values for T_l showed that deeper eutectics could be located near the gold terminal (gold-rich), however, the values of Tg increases as more Cu is added to the alloy. Both Tg and Tl contribute to the values of Trg. In this case, the effect of Cu addition on Tg prevails, as shown by the rise of Trg.

[F] The cooling rate of the splat quenched sample is calculated using a high-speed video camera. To splat a liquid droplet, copper pistons take about 0.5-2 milliseconds to complete the process. The temperature is dropped from 1300 K range to room temperature (300 K). A rough calculation of the cooling rate yields 1000 K per 0.001 seconds, or equivalently, 10^6 K/sec. The relationship between sample thickness and critical cooling rate can also be found in Appendix B.

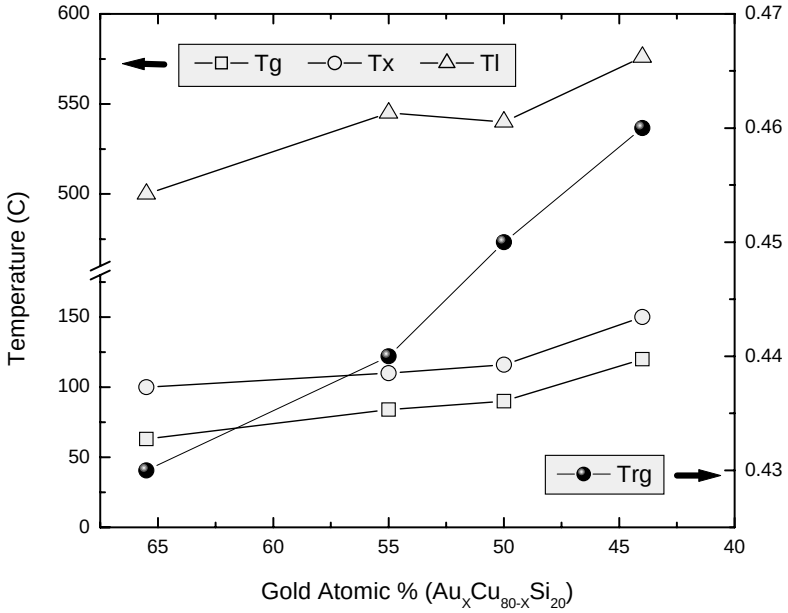

Figure II-14: The effect of copper addition in Au-Cu-Si ternary alloys. The Si content is fixed at 20 atomic%. Three characteristic temperatures T_l, T_x and T_g are plotted with respect to the left axis. The right axis corresponds to calculated Trg values (unitless).

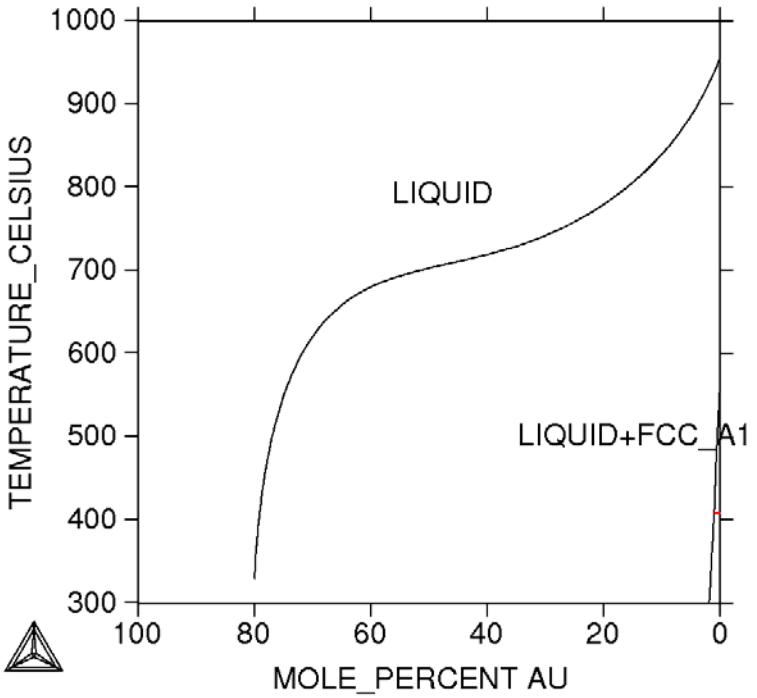

Figure II-15: Thermo-Calc prediction of the liquidus for the same Au-Cu-Si ternary alloy when Si content is fixed at 20 atomic%. The horizontal axis represents the X values in $Au_XCu_{80-X}Si_{20}$. The experimental results are plotted in Figure II- 14.

3.4.2 Slow Quenching Studies – Stage II Development

The alloy compositions of nominal glass formers found in the rapid quenching stage were systematically adjusted for improved GFA. A few chosen compositions with decent GFA are then tested by casting at slower cooling rate (or thicker geometry). The cast specimens then underwent similar DSC and x-ray diffraction analyses.

In order to optimize the alloy compositions to achieve the "bulk" cast level of GFA, a more careful investigation of the competing phases that crystallize in the amorphous matrix should be conducted. In order to prevent such crystalline formation, alloy developers could (1) shift the composition away from the phase that crystallizes easily towards the phases that exhibit more undercooling, and (2) introduce another element to upset the formation of the culprit crystalline phase, for example, introducing an element of slightly larger or smaller atomic radii to strain the competing crystalline lattice.

Scanning Electron Microscopy (SEM)[G] and Energy Dispersive Spectrometry (EDS)[H] are valuable tools for identifying the compositions of various phases found in cast specimens. The discussion on SEM and EDS analysis techniques can be found in the next section.

[G] At Caltech, we usually use a LEO 1550 VP Field Emission (FE) SEM equipped with in-lens, below-lens, and variable pressure Secondary Electron (SE) detectors, as well as a Robertson-type Back-Scattered Electron detector.

[H] In conjunction with the LEO FE SEM, an Oxford INCA Energy 300 X-ray EDS system was employed for compositional analysis.

3.5 SEM / EDS Analysis

3.5.1 Locating the Low Melting Liquid and Finding its Composition

Time and again the splatted samples or cast strips did not contain a detectable glass fraction, but they could contain low melting phases or deep eutectics. DSC results usually reveal multiple melting events; the phase that exhibits the lowest melting event generally deserves further investigation. For instance, the $Au_{65}Sn_{24}Sb_{11}$ was made based on a Thermo-Calc prediction. The alloy was cast in 0.5 mm thick strip and its microstructure (BSE) is shown in Figure II-16.

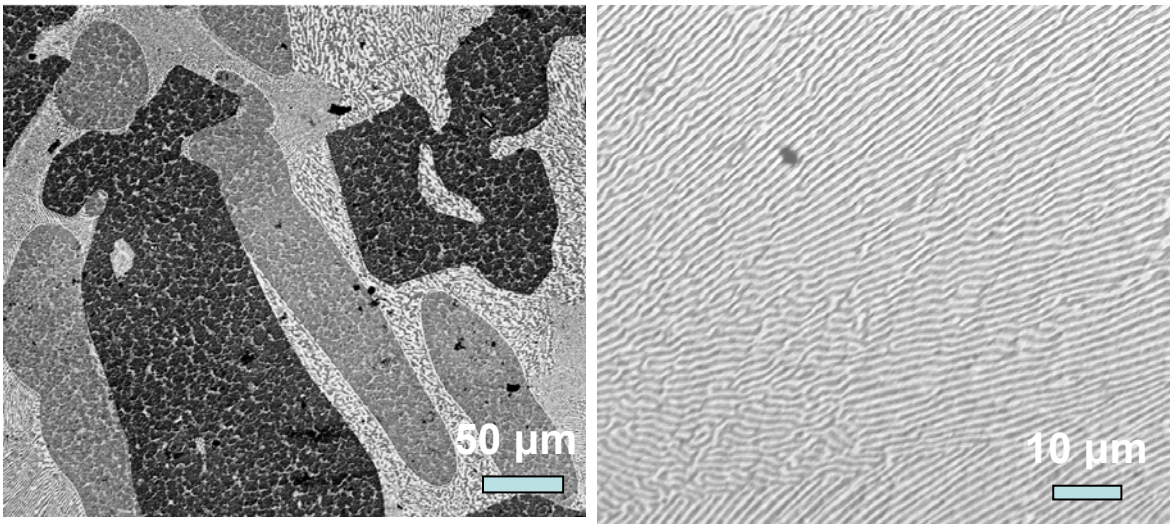

Figure II-16: Left BSE image shows at least three compositional contrast phases found in $Au_{65}Sn_{24}Sb_{11}$ cast strip (0.5 mm thick). Right BSE image shows fine sub-micron eutectic microstructure.

Using EDS composition analysis in conjunction with x-ray diffraction and DSC analysis, the darkest phase was identified as a $AuSb_2$, the medium-gray phase was AuSn,

and the last phases that precipitated out were confirmed to be a eutectic. The alloy of eutectic composition was then made and the DSC constant heating scan revealed only one melting event with a narrow and strong heat signal.

In another attempt, Loffler et al. conducted a novel experiment to locate the lowest melting phase by using centrifugal processing techniques [30]. By applying ultra-high gravity and slow cooling to the melt, the primary crystals would precipitate and sediment to the ends. Subsequently, other crystals that exhibit slightly better undercooling would precipitate as the temperature slowly drops further. Binary and ternary eutectic phases then would precipitate last and, therefore, could be located near the middle of the sample.

3.5.2 Locating the Competing Phase(s)

In a similar approach, SEM and EDS analysis help alloy developers to identify a few phases that precipitate last, right before the last remaining of the melt is vitrified. An amorphous matrix decorated with fine crystals is one common microstructure found in a good glass former that was quenched at a cooling rate slightly less than Rc. The crystallization event is just "started" when the melt passes through the nose of a TTT diagram in the time-temperature space.

$Au_{55}Cu_{25}Si_{20}$ was cast into 0.5 mm and 1 mm thick strips. The specimens were almost completely amorphous. The microstructure of such alloy, shown in Figure II-17, comprises of mostly fine particles (1-2 microns) embedded in the amorphous matrix. SEM and EDS analysis reveals that these "dark" particles are mostly copper silicides and

cubic silicon (more than 90 atomic% Si). As a result, both Cu and Si content must be reduced in the next set of alloy formulations.

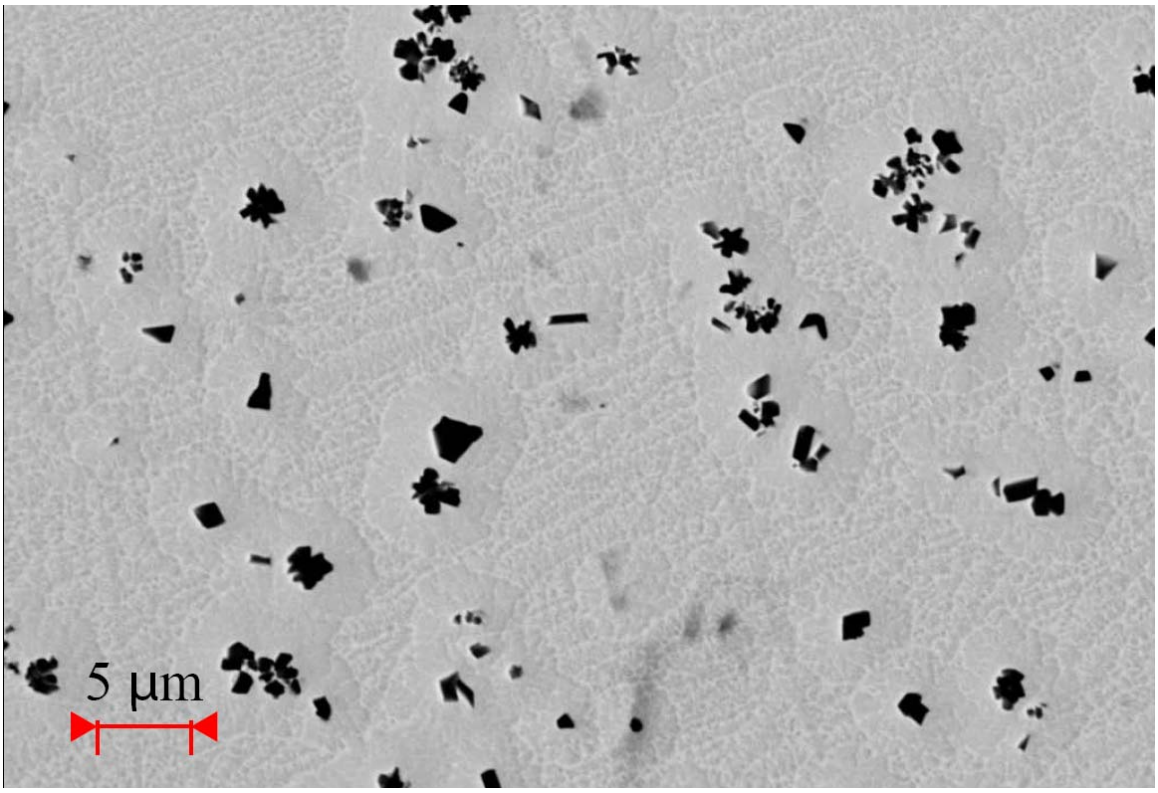

Figure II-17: BSE image of $Au_{55}Cu_{25}Si_{20}$ cast strip (1 mm thick). Copper silicides and silicon precipitates embedded in the amorphous gold matrix were identified using EDS.

After several such alloy synthesizing iterations, we narrowed down the composition to $Au_{43}Ag_{10}Pd_6Cu_{22}Si_{19}$. The alloy composition was formulated around a few concepts: (1) Si content must be reduced to avoid the cubic silicon precipitates, (2) Cu content must also be reduced to shift the composition away from copper silicide formation, and (3) Ag is added to "frustrate" the formation of copper silicides because Ag

and Cu are similar (both are Face Centered Cubic and both are in group IB), but there are no intermediate silver silicides in the Ag-Si binary phase diagram.

Figure II-18 shows the BSE image resulting from a cast $Au_{43}Ag_{10}Pd_6Cu_{22}Si_{19}$ alloy (1 mm thick strip). The crystalline fraction has decreased dramatically. The remnant of Si, similar to that found in Figure II-17, indicates that Si content must be further reduced. There exists a new phase which is faint and resembles a "Y" shape. SEM and EDS analysis shows that the crystals are Pd_3Si. There was also evidence in the literature that this Pd_3Si crystal is very easy to precipitate. Mao et al. studied the solidification of $Pd_{77.5}Au_6Si_{16.5}$ in drop tube and noticed that Pd_3Si was the first crystal [31] to precipitate when the droplet diameter is large. Herlach et al. also observed that Pd_3Si were the first crystals that triggered the rest of the crystallization events in $Pd_{77.5}Cu_6Si_{16.5}$ [32].

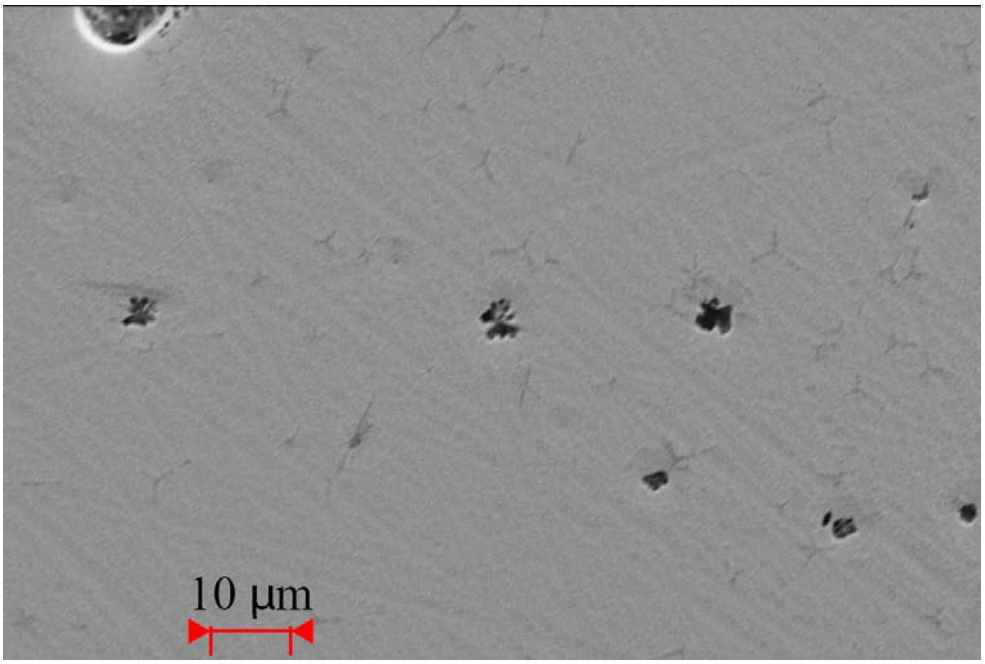

Figure II-18: BSE image of as-cast $Au_{43}Ag_{10}Pd_6Cu_{22}Si_{19}$ alloy (1 mm thick strip)

The glassy matrix was also analyzed for composition by EDS. The matrix contains approximately 5-6% Ag, 1.5-3% Pd, and 16-18% Si (atomic). After a few systematic iterations, the $Au_{49}Ag_{5.5}Pd_{2.3}Cu_{26.9}Si_{16.3}$ alloy was finally discovered. This alloy could be cast up to 5 mm fully amorphous. The results and properties this alloy family will be discussed in Chapter III.

4. Summary

A systematic approach to alloy design and development has been described. Alloy selection processes are now benefiting from faster and more reliable thermodynamic computations, MD simulations, and various modeling software. During the past few decades bulk metallic glasses have been discovered in a wide range of alloys. In some alloys a critical cooling rate to avoid crystallization as low as 0.005 K/s [33] and a critical casting thickness of up to 7 cm were reported [34] when heterogeneous nucleation was reduced. Such findings are just two of many scientific studies and discoveries that have led to meaningful insight into the physics of glass forming liquids, as well as the thermodynamics and kinetics of crystallization. Databases have become not only more complete but also more accurate, which is useful in development of BMGs.

Alloy development by design can be completed in a short time while the cost of alloy making is kept low. The systematic approach can be summed up in the following flow-chart (Figure II-19).

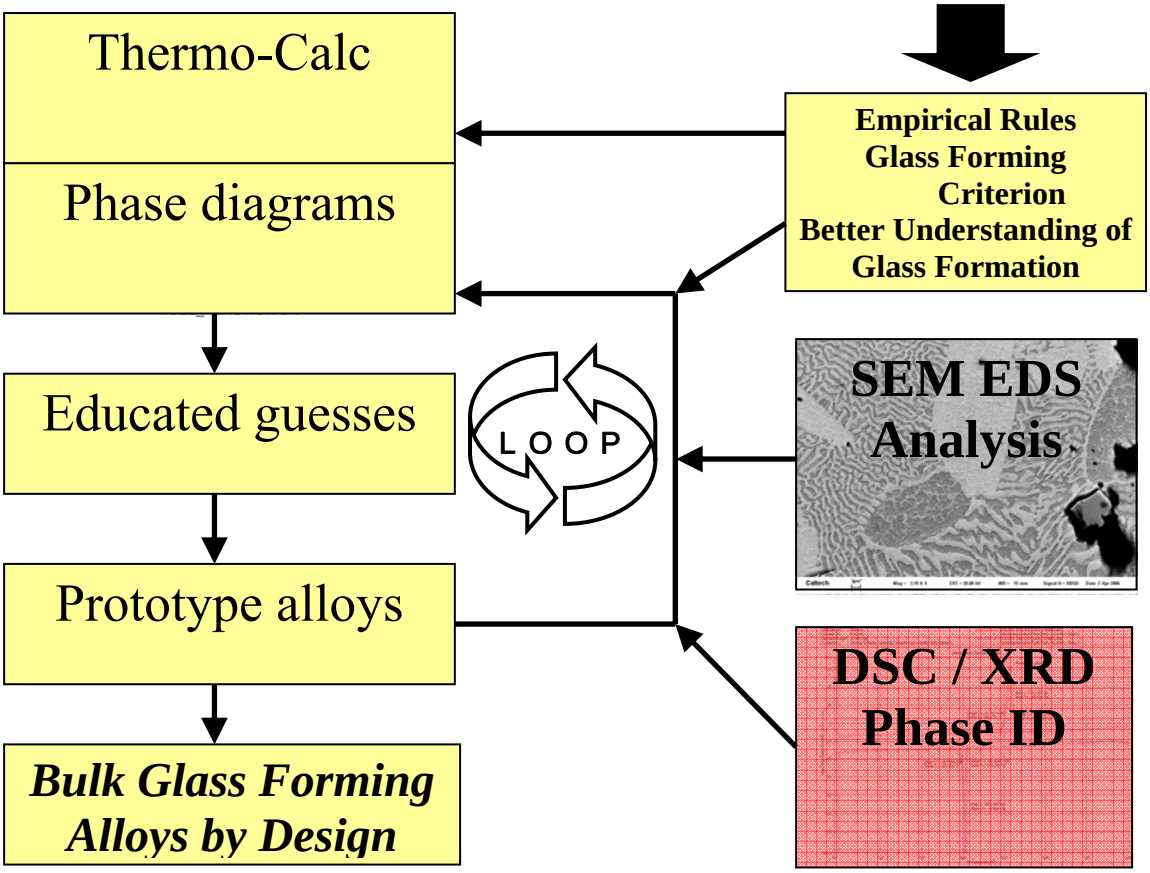

Figure II-19: Flow chart showing systematic alloy development. The processes are repeated (in the "loop") to attain a good bulk glass former or any alloy of interest.

References

[1] D. Turnbull, Contemporary Physics 10 (1969) 473.

[2] A. Inoue, K. Kita, T. Zhang, T. Masumoto, Materials Transactions Jim 30 (1989) 722-725.

[3] W. Hume-Rothery, H. M. Powell, Zeitschrift Fur Kristallographie 91 (1935) 23-47.

[4] W. Hume-Rothery, Atomic Theory For Students of Metallurgy, The Institute of Metals, London, 1969.

[5] J. R. Chelikowsky, Physical Review B 19 (1979) 686-701.

[6] T. Egami, Y. Waseda, Journal of Non-Crystalline Solids 64 (1984) 113-134.

[7] D. B. Miracle, Nature Materials 3 (2004) 697-702.

[8] H. J. Fecht, P. J. Desre, W. L. Johnson, Philosophical Magazine B-Physics of Condensed Matter Statistical Mechanics Electronic Optical and Magnetic Properties 59 (1989) 577-585.

[9] W. L. Johnson, H. J. Fecht, Journal of the Less-Common Metals 145 (1988) 63-80.

[10] H. J. Fecht, W. L. Johnson, Nature 334 (1988) 50-51.

[11] W. Kauzmann, Chemical Reviews 43 (1948) 219-256.

[12] P. R. Okamoto, N. Q. Lam, L. E. Rehn, Solid State Physics - Advances in Research and Applications, Vol 52 52 (1999) 1-135.

[13] R. B. Schwarz, W. L. Johnson, Physical Review Letters 51 (1983) 415-418.

[14] B. X. Liu, W. L. Johnson, M. A. Nicolet, S. S. Lau, Nuclear Instruments & Methods in Physics Research 209 (1983) 229-234.

[15] B. X. Liu, W. L. Johnson, M. A. Nicolet, S. S. Lau, Applied Physics Letters 42 (1983) 45-47.

[16] B. Lohwongwatana, J. Schroers, W. L. Johnson, Physical Review Letters 96 (2006) 075503.

[17] W. S. Lai, Q. Li, C. Lin, B. X. Liu, Physica Status Solidi B-Basic Research 227 (2001) 503-514.

[18] in: Massalski (Ed.) Binary Alloy Phase Diagrams, vol 3, ASM, Metals Park, OH, 1986, p. 2875.

[19] T. B. Massalski, Binary Alloy Phase Diagrams, ASM International, Materials Park, OH, 1990.

[20] 09Pri, in: Handbook of Ternary Alloy Phase Diagrams, ASM International, Metals Park, OH, 1995.

[21] TCCQ and TCW3, in: Thermo-Calc Software, Stockholm, Sweden, 2004.

[22] K. Suetsugu, A. Furusawa, M. Tanaka, H. Takano, H. Takehara, T. Horiuchi, K. Matsushige, Materials Transactions 47 (2006) 1082-1089.

[23] H. J. Lee, T. Cagin, W. L. Johnson, W. A. Goddard, Journal of Chemical Physics 119 (2003) 9858-9870.

[24] A. Inoue, K. Ohtera, T. Masumoto, Japanese Journal of Applied Physics Part 2-Letters 27 (1988) L736-L739.

[25] A. Inoue, K. Ohtera, Z. Tao, T. Masumoto, Japanese Journal of Applied Physics Part 2-Letters 27 (1988) L1583-L1586.

[26] M. C. Lee, J. M. Kendall, W. L. Johnson, Applied Physics Letters 40 (1982) 382-384.

[27] M. C. Lee, H. J. Fecht, J. L. Allen, J. H. Perepezko, K. Ohsaka, W. L. Johnson, Materials Science and Engineering 97 (1988) 301-305.

[28] A. Inoue, K. Kita, K. Ohtera, H. Kimura, T. Masumoto, Journal of Materials Science Letters 7 (1988) 1287-1290.

[29] A. Inoue, Y. Kojima, T. Minemura, T. Masumoto, Transactions of the Japan Institute of Metals 20 (1979) 468-471.

[30] J. F. Loffler, S. Bossuyt, A. Peker, W. L. Johnson, Philosophical Magazine 83 (2003) 2797-2813.

[31] Z. L. Mao, C. R. Li, H. Chen, X. Y. Shao, W. K. Wang, Journal of Materials Science 28 (1993) 4850-4854.

[32] D. M. Herlach, F. Gillessen, Journal of Physics F-Metal Physics 17 (1987) 1635-1644.

[33] J. Schroers, W. L. Johnson, Applied Physics Letters 80 (2002) 2069-2071.

[34] A. Inoue, N. Nishiyama, H. Kimura, Materials Transactions Jim 38 (1997) 179-183.